

Calculation of near-field scanning optical images of exciton, charged-exciton, and multiexciton wave functions in self-assembled InAs/GaAs quantum dots

Lixin He,¹ Gabriel Bester,² Zhiqiang Su,¹ and Alex Zunger²

¹Laboratory of Quantum Information, University of Science and Technology of China, Hefei, Anhui 230026, People's Republic of China

²National Renewable Energy Laboratory, Golden, Colorado 80401, USA

(Received 26 February 2007; published 12 July 2007)

The near-field scanning optical microscopy images of excitonic wave functions in self-assembled InAs/GaAs quantum dots are calculated using an empirical pseudopotential method, followed by the configuration interaction treatment of many-particle effects. We show the wave functions of neutral exciton X^0 of different polarizations and compare them to those of the biexciton XX^0 and the charged excitons X^+ and X^- . We further show that the exciton $X(P_h \rightarrow S_e)$ transition which is forbidden in the far-field photoluminescence has intensities comparable to those of $X(S_h \rightarrow S_e)$ transition in the near-field photoluminescence.

DOI: 10.1103/PhysRevB.76.035313

PACS number(s): 73.21.La, 71.35.-y, 78.67.Hc

I. INTRODUCTION

The three-dimensional confinement and nearly perfect isolation from its environment given in self-assembled semiconductor quantum dots (QDs) lead to “atomlike” electronic structure features manifested, among others, by μeV photoluminescence (PL) linewidths and a long coherence time. Such narrow and isolated levels open the way for potential applications using as single-photon emitters¹ and quantum-entangled sources.² At the same time, this allows fundamental studies of μeV -scale fine-structure splitting^{3,4} of exciton lines due to the electron-hole exchange interaction, spectral shift due to charged excitons,^{5–7} as well as multiexciton formation and decay. However, the spatial resolution of the traditional far-field spectroscopy is limited to $\lambda/2$, where λ is the wavelength of the probing light,⁸ much larger than the typical sizes of quantum dots (a few tens to about a hundred nanometers). Recently, it became possible to examine the inner structures of an exciton in the QDs and map out its spatial distribution using the near-field scanning optical microscopy (NSOM).^{9,10} In the far-field measurement, the transition intensity (within single-particle approximation) is proportional to $|\mathbf{p}|^2 = |\langle \psi_c | \mathbf{r} | \psi_v \rangle|^2$, where ψ_c and ψ_v are the conduction and valence band wave functions, respectively. While in the far-field measurements, the extent of the incident electromagnetic wave is such that its magnitude over the entire dot region can be safely taken as constant, in the near field, the electromagnetic profile of the tip $\xi(\mathbf{r} - \mathbf{r}_0)$, has an extent comparable to the size of the nanostructure and must be explicitly taken into account:

$$E(\mathbf{r}) = \xi(\mathbf{r} - \mathbf{r}_0) E_0. \quad (1)$$

In this case, the transition intensity is modulated by the shape of the external field, i.e., proportional to $|\mathbf{p}(\mathbf{r}_0)|^2 = |\langle \psi_c | \mathbf{r} \xi(\mathbf{r} - \mathbf{r}_0) | \psi_v \rangle|^2$. The resolution of NSOM can thus be much higher than⁹ $\lambda/2$, providing details on how the carriers are distributed in the quantum dots.

In a QD, the electron and hole wave functions can be approximated by products of envelope functions and Bloch functions. In the far-field measurement, the interband transitions obey two kinds of selection rules: one related to the Bloch part of the wave functions and one to the envelope

component of the wave functions. For example, from the four possible $S_h \rightarrow S_e$ excitonic transitions, two are bright and two are dark. The dark transitions are forbidden because the total angular momentum from the electron and hole *Bloch functions* parts is 2, and hence cannot be carried out by a single photon. In contrast, all of the eight $P_h \rightarrow S_e$ transitions are forbidden because a photon does not couple effectively to the *envelope* orbital angular momentum of the exciton. However, in NSOM, where the electromagnetic field is applied inhomogeneously only to a part of the dot, the global spatial symmetry is broken, thus altering the selection rules for the envelope functions and allowing transitions that are forbidden in far-field measurement.¹¹ We show here that the $P_h \rightarrow S_e$ transitions (which are far-field forbidden) have intensities in NSOM comparable to the $S_h \rightarrow S_e$ transitions. Furthermore, NSOM provides additional far-field allowed information about the Bloch part of the wave functions, which the far-field spectroscopy is lacking. For example, by comparing the transition intensities of different polarizations, one could determine the relative phase between $|X\rangle$ and $|Y\rangle$ components of the hole wave functions at each point. In contrast, in the far-field measurements, only the total polarization is measured and the wave function phase information of the Bloch part is lost.

Recently, Matsuda *et al.*¹⁰ have measured the near-field PL image of naturally occurring GaAs QDs formed spontaneously in narrow quantum wells. The enhanced NSOM spatial resolution is as high as 30 nm, much smaller than the measured QD sizes of ~ 200 nm. Unfortunately, the spatial resolution is limited because of the capping layers and is still too low for the self-assembled InAs/GaAs quantum dots.¹² In this paper, we predict via atomistic pseudopotential method the near-field PL images of the neutral exciton X^0 , the biexciton XX^0 , and the charged excitons X^+ and X^- in the much smaller self-assembled InAs/GaAs quantum dots, in anticipating future NSOM measurements.

II. METHODS

A. Far-field vs NSOM transition elements

To obtain the NSOM images, one must first calculate the single-particle wave functions for electrons and holes by solving the Schrödinger equations,

$$\left[-\frac{1}{2} \nabla^2 + V_{eff}(\mathbf{r}) \right] \psi_i(\mathbf{r}) = \epsilon_i \psi_i(\mathbf{r}), \quad (2)$$

where V_{eff} is the effective potential for the electrons in the quantum dots. For example, in an effective mass approximation (EMA), the effective potential is usually taken as two-dimensional harmonic potential, whereas in atomistic approaches,¹³ V_{eff} is a superposition of screened atomic pseudopotentials. Once one has the electron and hole single-particle wave functions, it is possible to construct the *many-particle* wave functions of the excitonic states, e.g., via the configuration interaction (CI) method,¹⁴ by expanding them as the linear combination of Slater determinants constructed from the single-particle electron and hole wave functions. The ground state can be described by a single determinant,

$$\Phi_0(\mathbf{r}_1, \sigma_1, \dots, \mathbf{r}_N, \sigma_N) = \mathcal{A}[\psi_1(\mathbf{r}_1, \sigma_1) \cdots \psi_v(\mathbf{r}_v, \sigma_v) \cdots \psi_N(\mathbf{r}_N, \sigma_N)], \quad (3)$$

where N is the total number of electrons in the system, σ is the spin index, and \mathcal{A} is the antisymmetrizing operator. The Slater determinants of neutral excitons $\Phi_{v,c}$ are obtained by promoting an electron at the valence state ψ_v to the conduction state ψ_c from the ground state Φ_0 , i.e.,

$$\Phi_{v,c}(\mathbf{r}_1, \sigma_1, \dots, \mathbf{r}_N, \sigma_N) = \mathcal{A}[\psi_1(\mathbf{r}_1, \sigma_1) \cdots \psi_c(\mathbf{r}_c, \sigma_c) \cdots \psi_N(\mathbf{r}_N, \sigma_N)]. \quad (4)$$

The α th neutral exciton wave function can be written as

$$\Psi_X^{(\alpha)} = \sum_{v=1}^{N_v} \sum_{c=1}^{N_c} C_{v,c}^{(\alpha)} \Phi_{v,c}, \quad (5)$$

where N_v and N_c are the numbers of valence and conduction states included in the expansion of the exciton wave functions, respectively. The coefficients $C_{v,c}^{(\alpha)}$ are obtained by diagonalizing the many-particle Hamiltonian H in the basis set $\{\Phi_{v,c}\}$.¹⁴

The far-field optical absorption of the α transition can be written as

$$\sigma(\omega) \propto \sum_{\alpha} |\mathbf{M}^{(\alpha)}|^2 \delta(\hbar\omega - E^{(\alpha)}), \quad (6)$$

where $\mathbf{M}^{(\alpha)}$ are the dipole matrix elements between initial many-particle state $|\Psi_i\rangle$ and the final state $|\Psi_f\rangle$,

$$\mathbf{M}^{(\alpha)} = \langle \Psi_f | \mathbf{r} | \Psi_i \rangle. \quad (7)$$

ω and $E^{(\alpha)}$ are the frequency of the external E field and the exciton transition energy, respectively. For a neutral exciton, the dipole matrix elements \mathbf{M} can be written in terms of single-particle orbitals as

$$\mathbf{M}^{(\alpha)} = \langle \Phi_0 | \mathbf{r} | \Psi_X \rangle = \sum_{v=1}^{N_v} \sum_{c=1}^{N_c} C_{v,c}^{(\alpha)} \langle \psi_v | \mathbf{r} | \psi_c \rangle, \quad (8)$$

where $\mathbf{p} = \langle \psi_v | \mathbf{r} | \psi_c \rangle$ are the single-particle dipole matrix elements between the conduction state ψ_c and valence state ψ_v . Similarly, one can calculate \mathbf{M} for charged excitons X^+ and X^- and biexciton XX^0 .

For NSOM, the external E field is applied locally at \mathbf{r}_0 modulated by the electromagnetic profile of the tip $\xi(\mathbf{r}-\mathbf{r}_0)$, which can be taken as a Gaussian function, e.g.,

$$\xi(\mathbf{r} - \mathbf{r}_0) = ce^{-|\mathbf{r} - \mathbf{r}_0|^2/a^2}, \quad (9)$$

where a is the width of the excitation field, much smaller than the dimension of the QD. For such local optical transition, we have to replace $\mathbf{M}^{(\alpha)}$ in Eq. (6) by

$$\mathbf{M}^{(\alpha)}(\mathbf{r}_0) = \sum_{v=1}^{N_v} \sum_{c=1}^{N_c} C_{v,c}^{(\alpha)} \langle \psi_v | \mathbf{r} \xi(\mathbf{r} - \mathbf{r}_0) | \psi_c \rangle, \quad (10)$$

equivalent to replacing in Eq. (8) the single-particle dipole moment $\mathbf{p} = \langle \psi_v | \mathbf{r} | \psi_c \rangle$ by the local single-particle dipole moment $\mathbf{p}(\mathbf{r}_0) = \langle \psi_v | \mathbf{r} \xi(\mathbf{r} - \mathbf{r}_0) | \psi_c \rangle$.

B. Evaluation of the NSOM transition elements: An atomistic approach

In the present work, we calculate the single-particle energy levels and wave functions in a atomistic screened pseudopotential scheme, where the total potential $V_{eff}(\mathbf{r})$ is a superposition of local, screened atomic pseudopotentials $v_{\alpha}(\mathbf{r})$ plus a nonlocal spin-orbit potential V_{SO} i.e., $V_{eff}(\mathbf{r}) = \sum_{n,a} v_{\alpha}(\mathbf{r} - \mathbf{R}_{n,a}) + V_{SO}$. The atomic positions $\{\mathbf{R}_{n,a}\}$ are obtained from minimizing the total bond-bending and bond-stretching elastic energy using the valence force field (VFF) model.^{15,16} The VFF model has been successfully applied to various semiconductor systems such as InAs/GaAs quantum well,¹⁷ GaInP alloys,¹⁸ and GaAsN alloys,¹⁹ and produced accurate structural parameters compared with the first-principles local density approximation calculations. The VFF parameters for the current system were obtained and well tested in Ref. 13. The atomistic pseudopotentials v_{α} ($\alpha = \text{In}, \text{Ga}, \text{As}$) are fitted to the physically important quantities of bulk InAs and GaAs, including band energies, band offsets, effective masses, deformation potentials, alloy bowing parameters, etc.¹³ Equation (2) is solved by expanding $\psi(\mathbf{r})$ as the “linear combination of bulk bands” (LCBB) of band index m and wave vector \mathbf{k} of material λ (=InAs, GaAs), strained uniformly to strain $\vec{\epsilon}$ (following Ref. 20), i.e.,

$$\psi(\mathbf{r}) = \sum_{\mathbf{k}} \sum_m c_{m,\mathbf{k}}^{(\lambda)} u_{m,\mathbf{k},\vec{\epsilon}}^{(\lambda)}(\mathbf{r}) e^{i\mathbf{k} \cdot \mathbf{r}}. \quad (11)$$

We use the lowest conduction bands for electrons and three highest valence bands for holes. Instead of calculating the local dipole matrix elements using Eq. (11), we project $\psi(\mathbf{r})$ onto (strained) Bloch functions of InAs at the Γ point in the Brillouin zone,

$$\psi(\mathbf{r}) = \sum_{m=1}^{N_p} f_m(\mathbf{r}) u_{\Gamma,m}(\mathbf{r}). \quad (12)$$

To simplify the notation, we drop the material index λ and strain index $\vec{\epsilon}$ in Eq. (12). Here, N_p is the number of the projection bands, which is usually much larger than the number of bands used in the LCBB equation. We found that $N_p = 9$ provides accurate projections. Here, $f_m(\mathbf{x})$ is the envelope

function for the m th band. The envelope functions are slow varying functions, compared to the Bloch functions. We can therefore separate the Bloch functions and envelope functions by dividing the volume into small regions, e.g., the eight-atom unit cells. In each unit cell, the envelope functions $f_m(\mathbf{r})$ and $\xi(\mathbf{r})$ can be treated as constants, i.e.,

$$\begin{aligned} \mathbf{p}(\mathbf{r}_0) &= \int d\mathbf{r} \psi_v^*(\mathbf{r}) \psi_c(\mathbf{r}) \mathbf{r} \xi(\mathbf{r} - \mathbf{r}_0) \\ &\approx \sum_{\mathbf{r}_i} \left[\sum_{m,m'} f_m^{*(v)}(\mathbf{r}_i) f_{m'}^{(c)}(\mathbf{r}_i) \mathbf{d}_{m,m'} \right] \xi(\mathbf{r}_i - \mathbf{r}_0), \quad (13) \end{aligned}$$

where \mathbf{r}_i is the position of i th cell and

$$\mathbf{d}_{m,m'} = \frac{1}{V} \int d\mathbf{r} u_{\Gamma,m}^*(\mathbf{r}) \mathbf{r} u_{\Gamma,m'}(\mathbf{r}) \quad (14)$$

is the dipole matrix element between bulk bands. In a periodic system, it is more convenient to use an alternative formula to calculate the dipole,²¹

$$\mathbf{d}_{m,m'} = \frac{1}{im\omega_{m,m'}} \langle u_{\Gamma,m} | \hat{\mathbf{p}} | u_{\Gamma,m'} \rangle. \quad (15)$$

If we assume high spatial NSOM resolution, i.e., $\xi(\mathbf{r}_i - \mathbf{r}_0) = \delta(\mathbf{r}_i - \mathbf{r}_0)$, Eq. (13) can be further simplified as

$$\mathbf{p}(\mathbf{r}_0) \approx \sum_{m,m'} f_m^{*(v)}(\mathbf{r}_0) f_{m'}^{(c)}(\mathbf{r}_0) \mathbf{d}_{m,m'}. \quad (16)$$

Combining Eqs. (10) and (16), we see that the shape of NSOM transition is the sum of the (multiband) envelope functions of the exciton weighted by the (single-particle) dipole matrix elements, i.e.,

$$\mathbf{M}^{(\alpha)}(\mathbf{r}_0) = \sum_{v=1}^{N_v} \sum_{c=1}^{N_c} C_{v,c}^{(\alpha)} \left[\sum_{m,m'} f_m^{*(v)}(\mathbf{r}_0) f_{m'}^{(c)}(\mathbf{r}_0) \mathbf{d}_{m,m'} \right]. \quad (17)$$

Previously, the NSOM images have been calculated via single-band EMA.^{11,22,23} In this approximation, the dipole moment \mathbf{d} is directly taken from bulk materials or from quantum wells,²³ while in our case, it is calculated for nine bands in Eq. (15) and is specific to the nanostructure considered. In the single-band EMA, only the envelope part of the information is kept in the calculation of NSOM images, whereas detailed information associated with the Bloch functions, such as polarizations, is lost. In the more advanced $\mathbf{k} \cdot \mathbf{p}$ methods, one includes the heavy-hole, light-hole, and spin-orbit bands at the Γ point of the Brillouin zone in the calculations. For the direct gap materials, these approximations give qualitative right results, but for indirect gap materials, such as Si quantum dots, one needs to include more bands.

III. RESULTS AND DISCUSSION

A. Excitonic spectrum of the InAs/GaAs QD

We performed calculations on a lens-shaped InAs/GaAs quantum dot with 27.5 nm base diameter and 3.5 nm height.

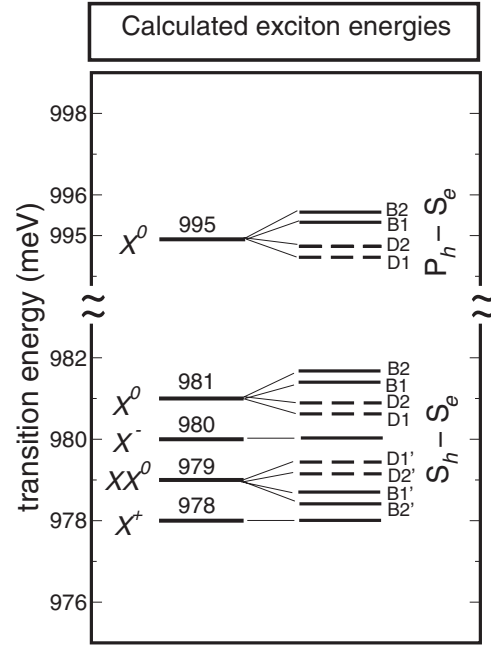


FIG. 1. The exciton energies of the lowest neutral exciton X^0 , the charged excitons X^+ and X^- , and the biexciton XX^0 of self-assembled InAs/GaAs QD with base $b=27.5$ nm and height $h=3.5$ nm. The right hand side shows the schematic energy levels of fine-structure splittings of each state. The solid lines ($B1$, $B2$, etc.) denote bright (B) states, whereas the dashed lines ($D1$, $D2$, etc.) denote dark (D) states.

The calculated transition energies of the exciton X^0 , the charged excitons X^+ and X^- , and the biexciton XX^0 of $S_h \rightarrow S_e$ transitions are given in Fig. 1. The neutral X^0 has the largest transition energy of 981 meV, while charged excitons and biexcitons have 1–3 meV redshifts relative to the neutral exciton due to correlation effects,²⁴ in agreement with experiments.^{5,6} For the neutral exciton, the exciton line splits into four lines shown on the right hand side of Fig. 1, as a consequence of the asymmetric electron-hole exchange energies.²⁵ The two low lying lines labeled $D1$ and $D2$ are “dark states” (forbidden due to the angular momentum selection rule of the Bloch part of the electron and/or hole states), whereas the upper two states ($B1$ and $B2$) are bright states. The calculated energy splitting between the bright and dark states is about 210 μ eV. The energy splitting between two dark states $D1$ and $D2$ is about 1 μ eV, whereas the splitting between two bright states $B1$ and $B2$ is about 10 μ eV, in agreement with previous calculations.²⁴ The low energy bright state $B1$ is polarized along the [110] direction, whereas the high energy state $B2$ is polarized along the [1̄10] direction. Although the biexciton XX^0 states themselves have no fine structures, the XX^0 to X transition exhibits fine structures. The charged excitons X^+ and X^- have no fine structures.

The energy of neutral exciton $P_h \rightarrow S_e$ transition is calculated here to be 995 meV, also shown in Fig. 1. Like the $S_h \rightarrow S_e$ transition, the $P_h \rightarrow S_e$ transition also splits into four fine structures. The two lower energy states are “forbidden” by the Bloch function angular momentum selection rule,

whereas the two high energy states $B1$ and $B2$ are allowed by the Bloch part. In the far-field measurement, the $P_h \rightarrow S_e$ transition is forbidden for the lens-shaped QDs due to the envelope function angular momentum selection rule (i.e., the overlap integrals between P_h and S_e envelope functions are very small). In practice, this transition is partially allowed,²⁶ but nevertheless very weak. However, unlike the selection rules for the Bloch functions, the envelope function angular momentum selection rule does not apply to NSOM, which involves only the local transition and does not feel the global spatial symmetry,¹¹ i.e., the overlap of P_h and S_e orbitals is not zero at a given point, and $P_h \rightarrow S_e$ transitions have intensity comparable to that of the $S_h \rightarrow S_e$ transitions. This will be further discussed in Sec. III C.

B. NSOM $S_h \rightarrow S_e$ transition for neutral exciton in the InAs/GaAs QD

The NSOM images of excitonic $S_h \rightarrow S_e$ transition of X^0 are shown in Fig. 2. We show the images of all fine-structure components $B1$, $B2$, $D1$, and $D2$ in Figs. 2(a)–2(d), respectively. The color bars indicate the magnitudes of transition intensities. We use arbitrary but equal units for the transition intensity in all subfigures. Each subfigure is composed of six panels showing the transition intensity of different polarizations. The first row in each subfigure shows the transition of polarization along the [100], [010], and [001] directions, whereas the second row of each subfigure shows the transition of polarization along the [1̄10] and [110] directions. The final panel is the total transition intensity, being the sum of intensities over polarization along the [100], [010], and [001] directions. (The sum of intensities over the [100] and [010] polarizations equals the sum over the [1̄10] and [110] polarizations.) We magnified the transition intensity by the factor shown on the upper-right corner of each panel, so the transition intensities in all subfigures can be in similar scale.

Considering first the total transition intensities, we notice that the transitions originate from a relatively small region around the center of the dot. The transition intensities of dark states $D1$ [Fig. 2(a)] and $D2$ [Fig. 2(b)] are about 2–3 orders of magnitude lower than those of bright exciton states $B1$ [Fig. 2(c)] and $B2$ [Fig. 2(d)], because they are forbidden due to angular momentum selection rule for the heavy hole to conduction band transitions. Therefore, the shapes of $D1$ and $D2$ are determined by the shape of higher bands [see Eq. (16)]. In contrast, the bright states $B1$ and $B2$ have S -like shape as expected. However, the NSOM images of $B1$ and $B2$ are not perfectly round, even though the lens-shaped QD we choose has cylindrical symmetry: we see that $B1$ is elongated along the [110] direction, whereas $B2$ is elongated along the [01̄0] direction.

We next discuss the NSOM images of different polarizations, focusing on the bright states. For far-field excitation, the low energy bright exciton $B1$ is calculated to be polarized along the [110] direction, whereas the high energy bright exciton $B2$ is polarized along the [1̄10] direction. This is clearly seen in the NSOM plots of Fig. 2 by comparing the [110] polarized plots to the [1̄10] polarized plot. However,

NSOM can provide much more information than the usual far-field measurement: The dipole moments have the following relations, $\mathbf{p}_{[110]} = (\mathbf{p}_{[100]} + \mathbf{p}_{[010]})/\sqrt{2}$ and $\mathbf{p}_{[1\bar{1}0]} = (\mathbf{p}_{[100]} - \mathbf{p}_{[010]})/\sqrt{2}$. Therefore, by comparing the NSOM images of different polarization, we can obtain the relative phases between $\mathbf{p}_{[100]}$ and $\mathbf{p}_{[010]}$ at each spatial point. For the bright states of $S_h \rightarrow S_e$ transitions, the relations are simple, i.e., $\mathbf{p}_{[100]}$ and $\mathbf{p}_{[010]}$ have almost fixed phases: 0 for the $B1$ state and π for the $B2$ state everywhere inside the QD. As we know, $\mathbf{p}_{[100]}$ corresponds to the $|X\rangle$ component in the hole Bloch functions, whereas $\mathbf{p}_{[010]}$ corresponds to the $|Y\rangle$ component. We therefore obtain additional information about the character of the hole Bloch functions as a function of position inside the QDs.

Figure 2 also shows the NSOM image of polarization along the [001] direction. For the bright exciton, the [001] components are significantly weaker than the components polarized in the (001) plane, and may not be detectable in practice. However, they are of theoretical interest. The polarization along the [001] direction comes from the emission of light hole. Therefore, the [001] image shows how the light-hole components are distributed in the QDs.

C. NSOM $P_h \rightarrow S_e$ transition for neutral exciton in the InAs/GaAs QD

Figure 3 depicts the $P_h \rightarrow S_e$ transitions, showing the two bright states ($B1$ and $B2$) out of the four fine-structure split states. Similar to Fig. 2, we show the NSOM images with polarization along the [100], [010], and [001] directions in the first row, and those with the [110] and [01̄0] polarizations and the total transition intensities in the second row. We see that the $P_h \rightarrow S_e$ transitions have intensities comparable to those of the $S_h \rightarrow S_e$ transitions. The shape of the total transition intensity of the $B1$ state somewhat differs from the intensity of the $B2$ state. However, both states have ringlike structures, and both states have two peaks in the [110] direction.

Each of the polarization-resolved plots looks like orbital p functions, although the transition peaks are oriented in different directions. For example, for the $B1$ state, the peaks of the [100] ([110]) polarized light are oriented along the [100] ([010]) direction, whereas the peaks of [110] ([1̄10]) polarized light are oriented in the [110] ([1̄10]) direction. As discussed in Sec. III B, we can obtain the phase relations of $|X\rangle$ and $|Y\rangle$ components in hole wave functions. We see that unlike the previous case involving an S_h wave function, in the Bloch part of the P_h wave functions, $|X\rangle$ and $|Y\rangle$ components have different phases at each point of the QDs. Similar results are found for the $B2$ state.

D. Comparison of NSOM of X^0 , X^+ , X^- , and XX^0 excitons in the InAs/GaAs QD

In Figs. 4(b)–4(d), we depict the NSOM images of the charged excitons X^+ and X^- and the biexciton XX^0 , respectively, and compare them to the $X^0S_h \rightarrow S_e$ transition from Fig. 4(a). We also plot the NSOM transition intensities along

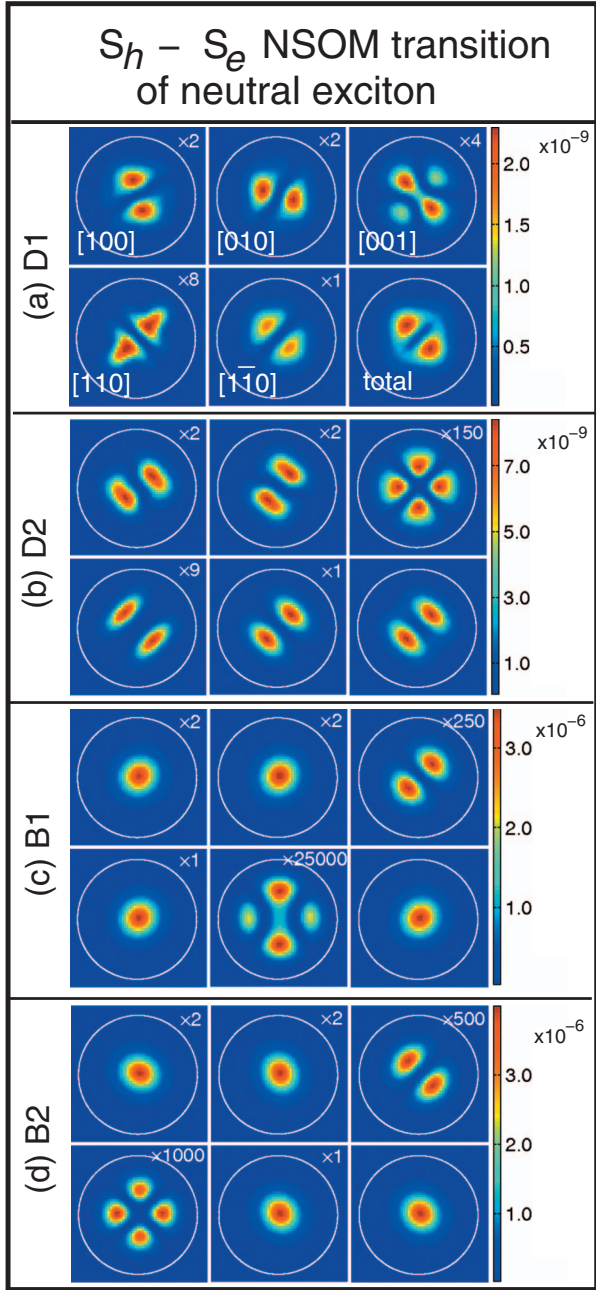


FIG. 2. (Color) The NSOM of excitonic $S_h \rightarrow S_e$ transitions in self-assembled InAs/GaAs QD with $b=27.5$ nm and $h=3.5$ nm, calculated from Eq. (17). The two dark excitons $D1$ and $D2$ are plotted in (a) and (b), respectively, whereas the two bright excitons $B1$ and $B2$ are plotted in (c) and (d). The unit of the color bar is arbitrary but equal for all subfigures. In each subfigure, there are six panels showing the transition intensities of different polarizations. In the first row, the polarizations are along the [100], [010], and [001] directions respectively, and in the second row, the polarizations are along the [110] and [$1\bar{1}0$] directions. The last panels show the sum of transition intensities of different polarizations. We magnify the transition intensities by the factors on the upper-right corner of each panel. The white circles (27.5 nm in diameter) show the boundaries the QDs.

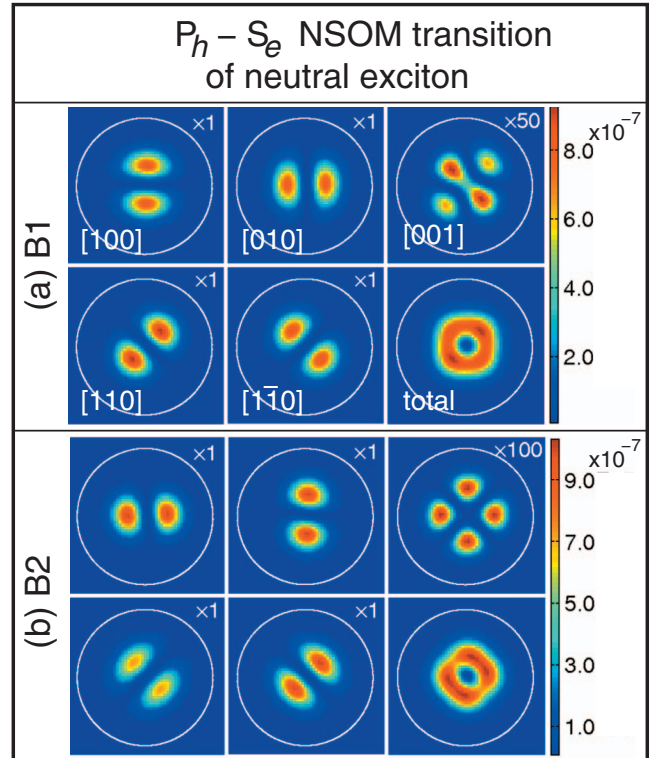


FIG. 3. (Color) The NSOM of excitonic $P_h \rightarrow S_e$ transitions (see Fig. 1) in self-assembled InAs/GaAs QD with $b=27.5$ nm and $h=3.5$ nm, calculated from Eq. (17) for (a) B1 and (b) B2 states. The unit of the color bar is arbitrary but equal for all subfigures. In each subfigure, there are six panels showing the transition intensities of different polarizations. In the first row, the polarizations are along the [100], [010], and [001] directions respectively, and in the second row, the polarizations are along the [110] and [$1\bar{1}0$] directions. The last panels show the sum of transition intensities of different polarizations. We magnify the transition intensities by the factors on the upper-right corner of each panel. The white circles (27.5 nm in diameter) show the boundaries the QDs.

the [110] direction in Fig. 5 for X^0 , X^+ , X^- , and XX^0 . The transition intensities of X^0 , X^+ , X^- , and XX^0 along the [1 $\bar{1}$ 0] direction are very similar to those along the [110] direction, and therefore are not plotted. We see that X^- has the strongest transition intensity, followed by X^0 , XX^0 , and X^+ . Even though the charged excitons and the biexciton have 1–3 meV redshifts relative to X^0 , they have shapes and sizes very similar to those of X^0 . The only noticeable difference is that X^+ has a slightly larger size than the other transitions. Therefore, the correlation effect due to the many-particle interactions is weak for the NSOM images in the self-assembled QDs. In Ref. 10, it was found experimentally and confirmed theoretically by single-band effective mass calculations^{22,23} that the radius of the biexciton NSOM signal is smaller than the radius of X^0 . In this calculation, we did not find a significant difference in size and shape between X^0 and XX^0 . However, the QDs used in the experiments (created by composition fluctuations in a quantum well) are much larger (\sim 200 nm in diameter) than the self-assembled QDs we studied here; therefore, the correlation effects are stron-

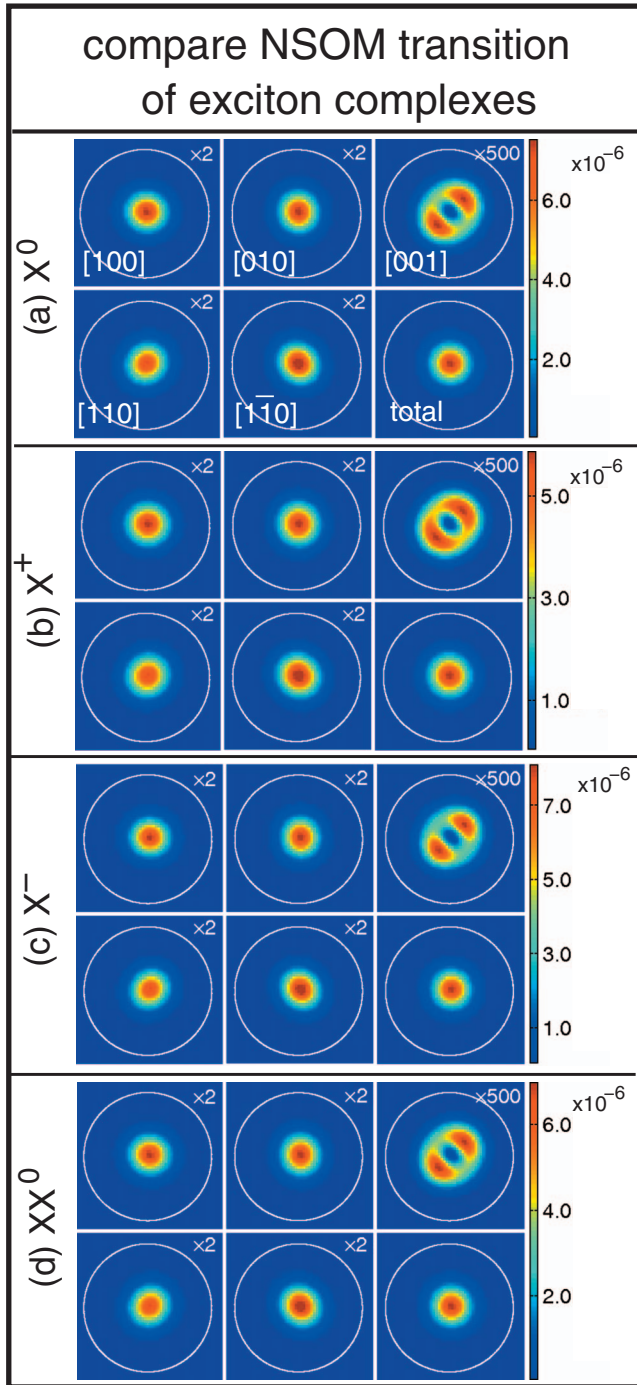


FIG. 4. (Color) The total NSOM images (sum over all fine structures) of excitonic $S_h \rightarrow S_e$ transitions (see Fig. 1) for (a) X^0 , (b) X^+ , (c) X^- , and (d) XX^0 in self-assembled InAs/GaAs QD with $b = 27.5$ nm and $h = 3.5$ nm, calculated from Eq. (17). The unit of the color bar is arbitrary but equal for all subfigures. In each subfigure, there are six panels showing the transition intensities of different polarizations. In the first row, the polarizations are along the [100], [010], and [001] directions, respectively, and in the second row, the polarizations are along the [110] and [$1\bar{1}0$] directions. The last panels show the sum of transition intensities of different polarizations. We magnify the transition intensities by the factors on the upper-right corner of each panel. The white circles (27.5 nm in diameter) show the boundaries the QDs.

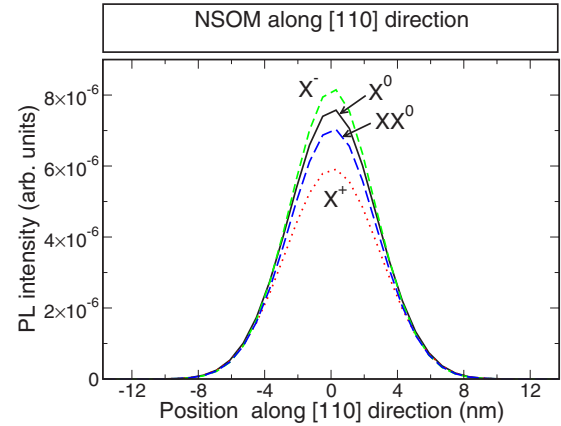


FIG. 5. (Color online) The NSOM transition intensities of X^0 (black solid line), X^+ (red dotted), X^- (green dashed), and XX^0 (blue dashed) along the [110] direction in self-assembled InAs/GaAs QD with $b = 27.5$ nm and $h = 3.5$ nm, calculated from Eq. (17). The origin is at the center of the dot.

ger. On the other hand, we ignored the continuum states in the CI calculation which may also underestimate the correlation effects to the wave functions.

IV. SUMMARY

We calculate the NSOM images of exciton complexes in self-assembled InAs/GaAs QD using an atomistic pseudopotential method followed by a configuration interaction treatment of the correlations. The NSOM images reveal the spatial structure of exciton and give information about the Bloch function character of the wave function, which remain unobserved in conventional far-field measurements. We show that the $P_h \rightarrow S_e$ transition, which is forbidden in the far-field PL measurement, has transition intensity comparable to that of the $S_h \rightarrow S_e$ transition in NSOM measurements. We also calculate the NSOM image of charged excitons X^+ and X^- and biexciton XX^0 and compare them with the image of X^0 . We found that the images obtained for charged excitons and the biexciton show features very similar to the ones obtained from the exciton decay.

ACKNOWLEDGMENTS

L.H. acknowledges the support from the Chinese National Fundamental Research Program (2006CB921900), the Innovation funds and “Hundreds of Talents” program from Chinese Academy of Sciences, and the National Natural Science Foundation of China (Grant No. 10674124). The work done at NREL was funded by the U.S. Department of Energy, Office of Science, Basic Energy Science, Materials Sciences and Engineering, LAB-17 initiative, under Contract No. DE-AC36-99GO10337 to NREL.

- ¹P. Michler, A. Kiraz, C. Becher, W. V. Schoenfeld, P. M. Petroff, L. Zhang, E. Hu, and A. Imamoglu, *Science* **290**, 2282 (2000).
- ²N. Akopian, N. H. Lindner, E. Poem, Y. Berlitzky, J. Avron, D. Gershoni, B. D. Gerardot, and P. M. Petroff, *Phys. Rev. Lett.* **96**, 130501 (2006).
- ³D. Gammon, E. S. Snow, B. V. Shanabrook, D. S. Katzer, and D. Park, *Phys. Rev. Lett.* **76**, 3005 (1996).
- ⁴M. Bayer, A. Kuther, A. Forchel, A. Gorbunov, V. B. Timofeev, F. Schäfer, J. P. Reithmaier, T. L. Reinecke, and S. N. Walck, *Phys. Rev. Lett.* **82**, 1748 (1999).
- ⁵A. Hartmann, Y. Ducommun, E. Kapon, U. Hohenester, and E. Molinari, *Phys. Rev. Lett.* **84**, 5648 (2000).
- ⁶D. V. Regelman, E. Dekel, D. Gershoni, E. Ehrenfreund, A. J. Williamson, J. Shumway, A. Zunger, W. V. Schoenfeld, and P. M. Petroff, *Phys. Rev. B* **64**, 165301 (2001).
- ⁷B. Urbaszek, R. J. Warburton, K. Karrai, B. D. Gerardot, P. M. Petroff, and J. M. Garcia, *Phys. Rev. Lett.* **90**, 247403 (2003).
- ⁸G. W. Bryant, *Appl. Phys. Lett.* **72**, 768 (1998).
- ⁹F. Flack, N. Samarth, V. Nikitin, P. A. Crowell, J. Shi, J. Levy, and D. D. Awschalom, *Phys. Rev. B* **54**, R17312 (1996).
- ¹⁰K. Matsuda, T. Saiki, S. Nomura, M. Mihara, Y. Aoyagi, S. Nair, and T. Takagahara, *Phys. Rev. Lett.* **91**, 177401 (2003).
- ¹¹U. Hohenester, G. Goldoni, and E. Molinari, *Phys. Rev. Lett.* **95**, 216802 (2005).
- ¹²K. Matsuda (private communication).
- ¹³A. J. Williamson, L.-W. Wang, and A. Zunger, *Phys. Rev. B* **62**, 12963 (2000).
- ¹⁴A. Franceschetti, H. Fu, L.-W. Wang, and A. Zunger, *Phys. Rev. B* **60**, 1819 (1999).
- ¹⁵P. N. Keating, *Phys. Rev.* **145**, 637 (1966).
- ¹⁶J. L. Martins and A. Zunger, *Phys. Rev. B* **30**, R6217 (1984).
- ¹⁷J. E. Bernard and A. Zunger, *Appl. Phys. Lett.* **65**, 165 (1994).
- ¹⁸A. Silverman, A. Zunger, R. Kalish, and J. Adler, *J. Phys.: Condens. Matter* **7**, 1167 (1995).
- ¹⁹L. Bellaiche, S. H. Wei, and A. Zunger, *Phys. Rev. B* **54**, 17568 (1996).
- ²⁰L.-W. Wang and A. Zunger, *Phys. Rev. B* **59**, 15806 (1999).
- ²¹D. Dragoman and M. Dragoman, *Optical Characterization of Solids* (Springer, Verlag, 2002).
- ²²S. V. Nair and T. Takagahara, *Phys. Rev. B* **55**, 5153 (1997).
- ²³U. Hohenester, G. Goldoni, and E. Molinari, *Appl. Phys. Lett.* **84**, 3963 (2004).
- ²⁴G. Bester and A. Zunger, *Phys. Rev. B* **68**, 073309 (2003).
- ²⁵G. Bester, S. Nair, and A. Zunger, *Phys. Rev. B* **67**, 161306 (R) (2003).
- ²⁶G. A. Narvaez and A. Zunger, *Phys. Rev. B* **74**, 045316 (2006).